

The Delineation of Mineralization and Hydrothermal Alteration Zones in Gitata Sheet 187, North Central Nigeria

Mam D. T.¹, Emmanuel E. U.², Abbass A. A.³ and Usman D. A.⁴

¹National Water Resources Institute, Mando Road Kaduna

^{2,3,4}Physics Department Federal University of Technology Minna

Corresponding author's e-mail: taweymam@gmail.com

ABSTRACT

This paper presents the delineation of potential mineralization and hydrothermal alteration zones within Gitata sheet (187) in north central Nigeria using airborne geophysical data. Aeromagnetic and aero radiometric data of high resolution covering the area were acquired and analyzed by mapping possible areas of mineralization, structures and hydrothermal alteration. The enhancement techniques applied to the data were the Analytic signal and Centre for Exploration Targeting (CET). The maps of radioelements and their ratios were used in the analysis. Structural analysis showed the dominant structural pattern within the study area to be NE-SW and NW-SE while the northwest and central portions of the study area were correlated with a strong analytic signal of 0.161 amplitude. Favorable mineralization zones were mapped from complex structural analyses and correlated with areas of high analytical signal within the northwest and central portion of the study area. Inspection of aero radiometric maps helped to delineate hydrothermal alteration zones that predominate in undifferentiated older granite, Migmatite and Gneiss followed by some occurrences within the porphyritic granites in the eastern part of the study area and the Pelitic schist/Muscovite having some occurrence of the hydrothermal zones delineated. Areas with strong analytic signal and complex structures are considered to be favorable for mineralization as mineralization fluids may have solidified in the structures and also alter the composition of the host and adjacent rocks.

Keywords: Mineralization, Hydrothermal Alteration, Complex Structural Analysis, Geomagnetic Declination

Introduction

The role of aeromagnetic method in mineral exploration varies from delineation of structures like faults, folds, contacts, shear zones and intrusions to automated detection of porphyry and favorable areas of ore deposits Elkhateeb and Ahmed (2018). These structures play important roles in the localization of mineralization. In comparison with other airborne geophysical methods, gamma-ray spectrometric method shows more success in mapping surface geology (Darnley *et al.* 1989). In addition, it is helpful in deducing some structures that may not be recognized through analyzing potential field methods. Also, this method is more useful and accurate in the identification of hydrothermal alteration zones and their detection. Shives *et al.* (1997) recommend the use of eTh/K ratio as the best

indicator of recognizing potassic alteration zones. Several studies have also been conducted for identifying alteration zones (Elkhateeb and Abdellatif, 2018; Feebrey *et al.* 1998; Irvine and Smith 1990; Morrell *et al.* 2011; Wemegah *et al.* 2015). As such, this work is aimed at delineating prospective mineralization and hydrothermal zones within Gitata (sheet 187) Nigeria.

Location and Topography of the Study Area

The area of study falls within two states and the federal capital territory. These are Kaduna and Nasarawa states (Figure 1). It is bounded by latitude 9° N to 9° 30' N and Longitude 7° 30' E to 8° E. The study area falls within the north central Nigerian basement complex and extend from south of Abuja to east of Ungwar Alura in the south and from Kwoi town to west of Kagarko in the north.



Fig. 1. Location of the study area.

The topography of the area provided by Shuttle Radar Topography Mission (SRTM) ranged from 255.957 m for the low elevated part of the area with the western part of the study area down to the southern end (Figure 2) to areas having elevation above 772.57 m in the high elevated part of the map specifically around north-east corner, the southern part of the map to north-west and the western end down to the south (Figure 2).

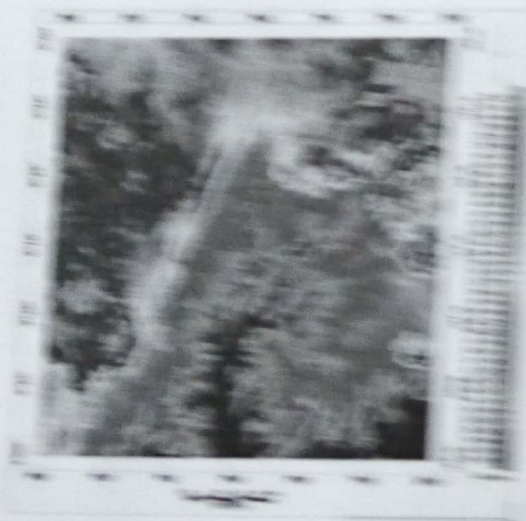


Fig. 2. SRTM Map of the Area with Topography Variation.

Geology of the Study Area

The study area is underlain by the basement complex rocks (Figure 3) (NGSA, 2006). The basement complex rocks in the area are composed of low, medium and high grade gneiss (Amphibole, MAFG), the Sialic Belt Metasedimentary and Metavolcanic rocks, the Older Gneiss (Pre-African granulite). The Metasedimentary complex is Neoproterozoic to Palaeoproterozoic (1947 No. 200) and is composed of rhyolite and gneiss. Metavolcanic rocks consist of andesite and basaltic and gabbroic rocks occupying the central part of the study area from south to the north (Figure 3). The orthogneiss of Pre-African granulite are Pre-African (664-720 Ma) in age and consist mainly of orthogneiss, gabbro, granite and gneiss occupying the south-western part of the map and Sialic Belt gneiss and orthogneiss, granite.

Both the migmatites and gneisses were deformed and intruded by the older granites (or Pan-African granitoids) during the 600-200 Ma Pan-African episodes. Schists within the study area occupy the western portion of the

map (Figure 3), down to the south and other smaller occurrences of the Schists within the north, northeast, southeast, south and central portion of the map (Figure 3).

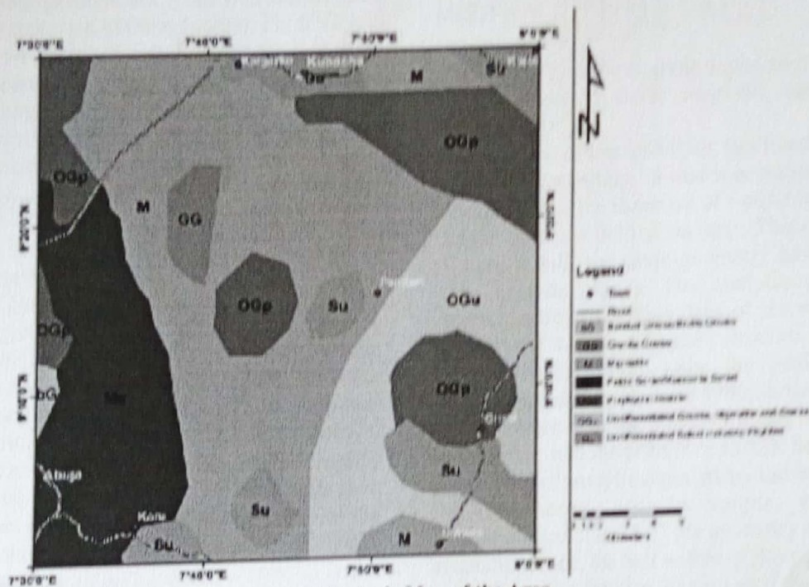


Fig. 3 Geologic Map of the Area

Materials and Methods

High-Resolution Aeromagnetic Data (HRAD) and airborne radiometric data (equivalent thorium and percentage potassium data) of part of central Nigeria were acquired from the Nigeria Geological Survey Agency (NGSA). The data covered an area of about 55 x 55 km² (bounded by latitudes 09° 00'-09° 30' N and longitudes 07° 30'-08° 00' E). The aeromagnetic and radiometric surveys were carried out between 2005 and 2009 by Fugro Airborne Surveys for the NGSA. The data were recorded at an interval of 0.1 s (~7.5 m) for magnetic measurements and 1.0 s (~75 m) for radiometric measurements. The airborne surveys were flown in the NW-SE direction perpendicular to the major geological trends in the area, with flight line spacing of 500 m, terrain clearance of 80 m, and tie line spacing of 2000 m in NE-SW direction. Based on the

very short recording interval, lower survey flight height (80 m), and narrower flight line spacing, the resolution of the anomalies is immensely higher than the conventional high-altitude air borne surveys. All essential data corrections, including the removal of IGRF values, were done by Fugro Airborne Surveys. The maps were processed using the Oasis Montaj software version 8.4. The TMI was reduced to the equator, using magnetic inclination and declination of the centre point of the study area, so that anomalies observed would be directly positioned on their respective causative source bodies. Unwanted signals which include the regional fields were removed by upward continuing the Reduced-to-Equator (RTE) map to a height of 30 km, where the resultant grid was subtracted from the RTE grid to obtain the residual grid displays as map. Analytic Signal (AS) source

edge mapping technique was applied on the filtered residual data to delineate the magnetic source boundaries. The amplitude of analytic signal within the study area was achieved by calculating the square root of sum of squares of magnetic gradient x , y and z functions using grid-derivative of minimum. The 2D grid analysis approach was employed in this study to identify linear features within the aeromagnetic data, then local structural complexity was analyzed using the spatial associations between adjacent linear features. Finally, lineaments or structures were detected based on local feature (Holden et al. 2008). Then the spatial associations of the detected lineaments were analyzed to construct two maps corresponding to each of the structural complexity cases, namely a feature intersection corner occurrence density map and a feature orientation entropy map. These maps show the occurrence of these structural scenarios, which aided a manual prospectivity analysis. The radiometric data which comprise both the potassium potassium and equivalent thorium maps were displayed and ratio of the maps which is $\%K/Th$ was obtained by the expression

$$\frac{\%K}{Th} = \frac{\%K \text{ grid}}{Th \text{ grid}} \quad (9)$$

using the grid and expression function of Oasis Montaj version 8.4 which is very useful in the mapping of hydrothermal alteration zones. The structural map produced from the analysis of aeromagnetic data using CFT were integrated with the hydrothermal alteration zones delineated from Kibuki's map to produce a composite proposed geologic map of the area.

Analytic Signal Method

The analytic signal of total magnetic intensity data (TMI) has much less sensitivity to geomagnetic field inclination than the original TMI data and offers a way of analyzing low latitude magnetic fields without the RTP operator's concerns. Analytic signal is a common gradient enhancement which is related to the magnetic fields by the derivatives. Roest et al. (1992), showed that

the amplitude of the analytic signal can be determined from the three orthogonal gradients of the total magnetic field using the expression:

$$A(x, y) = \sqrt{\left(\frac{\partial T}{\partial x}\right)^2 + \left(\frac{\partial T}{\partial y}\right)^2 + \left(\frac{\partial T}{\partial z}\right)^2} \quad (10)$$

where $A(x, y)$ is the analytic signal amplitude at (x, y) and T is the magnetic intensity (Roest et al. 1992).

In the context of interpretation, this function is extremely interesting, in that it is completely independent of the direction of magnetization and the magnetic field of the earth. This means all features with the same geometry have the same analytic signal. The analytic signal shows maxima over the edges of the source body even if the magnetization direction is not vertical. Furthermore, since the poles of analytic signal functions are symmetrical and occur directly over the edges of linear bodies and directly over the corners of linear bodies, the analysis of analytic signal maps and images can, in theory, provide simple, easily understood indications of the geometry of the magnetic source, the full width of linear bodies can be linearly related to the length of the poles source are vertical magnetic sources (Roest et al. 1992). The analytic signal, although often more discontinuous than the simple horizontal gradient, has the property that it generates a maximum directly over linear bodies as well as their edges. The width of a maximum, or ridge, is an indicator of length of the corner, as long as the signal arising from a single corner can be resolved.

Centre for Exploration Targeting (CET)

Centre for Exploration Targeting (CET) is a suite of algorithms that provide enhancement, lineament detection and structural complexity analysis functionalities for potential field data (Cox et al. 2009; Holden et al. 2008). This technique automatically delineates lineaments and identifies promising areas of ore deposits within the study area using total magnetic intensity (TMI) data through outlining regions of convergence and structural element

divergence using several statistical steps including textural analysis, lineament detection, vectorization and complexity analysis to generate contact occurrence. The contact occurrence areas show junction areas (point where two lineaments meet) and high linear density areas. These areas are favorable for hosting interest-bearing deposits and could be further explored (Geosoft 2012). Furthermore, CET grid method also enhances discontinuity zones in magnetic data and highlights critical magnetic intensity irregularities. Structures are founded in the data by finding several zones of texture in the restricted magnetic response before examining axes of symmetry. These axes are likely to detect straight abruptness in magnetic intensity. Areas of magnetic discontinuity are often due to and exhibited by rock edges, elongated structures, and intrusions that are important to assuming the geological framework of an area (Kovesi 1991). Zones of magnetic discontinuity are expressed by the use of texture enhancement in the form of the skeletal structure. The output data defines each region of the discontinuity zones as skeletal line fragments which belong to each of them, showing the deviations within the structural characteristics clearly in the directions and offsets (Kovesi 1997).

This technique makes use of the following actions:

I. Texture Analysis Enhancement (Standard Deviation)-determines magnetic discontinuity related with regions of complicated textures. Standard deviation enables the local variation to be delineated in the data. This calculates the standard deviation of the data values within the local neighborhood at every point in the grid. Important features often show a high variability with respect to the background signal. For a window containing N cells with a mean value of μ , the cell's standard deviation σ of the cell values

$$S = \sqrt{\frac{1}{N} \sum_{i=1}^N (x_i - \mu)^2} \quad (3)$$

When interpreting the results, values which approximate zero indicate very little variation, whereas high values indicate large variation.

II. Phase Symmetry – Utilizes the texture enhancement results for distinguishing zones of lateral discontinuity.

III. Detection of Structures – Uses the results of phase symmetry to reduce the discontinuities including zones into line-like structures.

IV. Complex structural Analysis (Contact Occurrence Density and Orientation Entropy Maps)

The feature intersection density map is generated by a collection of selected intersections, which include crossings, junctions and corners of the identified line segments; first, by extending each line segment to infinity, all projected intersection points are determined from all pairs of line segments. Candidate contact points are the intersections of those extended line segments. Selection is determined for each candidate using the distance between the intersection point and their respective line segments, and the angle between the line segments. If a projected intersection point lies within a permissible separation distance of say 250 m on one or both of the line segments, then the point is selected as a candidate. Those candidate points will be further analyzed to remove line segment intersections of similar orientations. Using aeromagnetic data, a linear anomaly can appear as broken feature due to incomplete sampling of magnetic field variations in the magnetic field (Holden *et al.* 2012). These features that may belong to the same anomaly may exhibit similar orientations, and is filtered by a threshold angle deviation i.e. removal of candidate points from line segments with a deviation angle less than threshold. Figure 4 shows the processes of elimination for the candidate intersection.

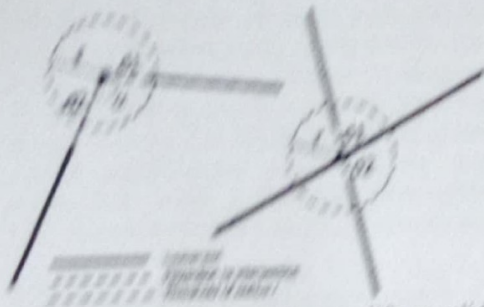


Fig. 4 Two example cases that qualify as valid intersection points. For the projected distances to the intersection d_1 and d_2 , either d_1 or d_2 , or both are less than the threshold distance of r . Also, in the first case, the angle α between the line segments also indicates that they are non-parallel (Holden et al. 2012).

The contact occurrence density map is constructed using the following processes.

Firstly, given the final collection of intersection points, each point contributes a Gaussian $G_i(x, y, \sigma)$ for a σ determined by the image resolution and scale of the local region being analysed for structural complexity. This causes areas with many valid intersection points to be supported by many Gaussian contributions. The resulting structural complexity heat map $H(x, y)$ is given by summing all Gaussians:

$$G_i(x, y) = \frac{1}{\sqrt{2\pi}\sigma} e^{-\left(\frac{x-x_i}{\sigma} + \frac{y-y_i}{\sigma}\right)^2} \quad (4)$$

$$H(x, y) = \sum_{i=0}^n G_i(x, y, \sigma) \quad (5)$$

Orientation entropy (diversity) map provides information about variability in feature orientations within a local neighborhood. As with the feature intersection density map, each identified texture ridge feature is represented as a collection of line segments.

These line segments are then used to calculate the orientation entropy (i.e., diversity) by measuring how many different orientations are represented by the line segments within each neighborhood. The range for all possible line

orientation (i.e., between 0° and 180°) is divided into a number of bins. For each line segment, the orientation is firstly quantized by determining the bin within which the orientation lies. Then for a given neighborhood, we measure the diversity of orientations of the line segments by determining how many different bins are represented within the neighborhood.

The traditional entropy measure (Parker 1997) was adapted to compute information for each pixel of the raw orientation diversity image, that is:

$$E = -\sum_{i=1}^n (p_i * \log(p_i)) \quad (6)$$

where n is the number of orientation bins, and p_i is the observed percentage of pixels with orientation i within the $r \times r$ neighborhood surrounding the pixel (x, y) , out of the total number of pixels corresponding to line segments. The size of the neighborhood controls the spatial extent to which the distribution of structures is examined. For example, given a pixel with a spatial resolution of 50 m, a square 60×60 pixel neighborhood represents a 3×3 km area. The appropriate choice of the window size depends on the spatial resolution of the data and the perceived size of the structures that are allowing movement of the mineralizing fluid. Finally, Gaussian smoothing is applied to the orientation diversity image to improve the visualization of the heat map (Holden et al. 2012).

Results and Discussions

The total magnetic intensity map (Figure 5a) reveals variation in magnetic signatures within the study area from south to north and from the east to west. The map (Figure 5a) is produced in different colors, pink to red and green to blue depicting positive anomaly (magnetic high) and negative anomaly (magnetic low). The magnetic intensity values within the area ranges from 32940.145 nT minimum to 33092.812 nT maximum with total number of 2,428,540 data points. The area is marked by both magnetic lows and high closures which could be attributed to the difference in the

lithology of the rocks within the study area and difference in the magnetic susceptibility of the rocks within the area, variation in depth to magnetic source within the study area and degree of strike. The magnetic high that occurs around south-eastern portion of the map coincided with the older granitoids (undifferentiated older Granite, Migmatite and

gneiss), undifferentiated schist with phyllites, porphyritic Granite and the Migmatite (Figure 3). The magnetic low that occurs around the north central portion of the study area coincided with the Migmatite, undifferentiated schist with phyllites, and the porphyritic Granite.

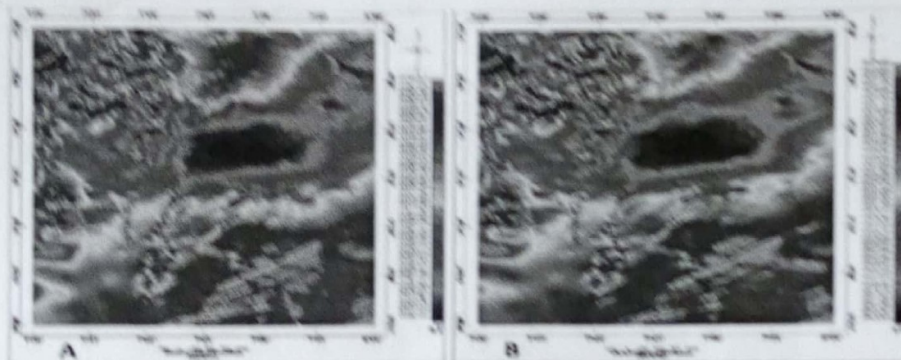


Fig. 5 (a) Total Magnetic Intensity and (b) Total Magnetic Intensity Reduced to Equator Maps

Also, around the north-western portion of the map, there is an observed occurrence of mixture of both magnetic low and high that could be attributed to the presence of deep-seated structures and possibly igneous intrusions.

To realign the anomalies and have their peaks symmetrically centered over their corresponding sources because the study area is very close to the equator. Total magnetic intensity grid of the study area was reduced to magnetic equator grid with geomagnetic inclination of -5.298 and geomagnetic declination of -1.995 of the central point of the study area to get the actual position of the magnetic anomalies without losing any geophysical meaning (Figure 5b). The RTE map (Figure 5B) when compared with the TMI (Figure 5a) map shows slight variation in their magnetic intensities. The RTE map have magnetic intensities that varies from 32938.934 nT minimum to 33076.690 nT maximum compared to TMI map where the magnetic intensity values within the area ranges from 32940.145 nT minimum to

33092.812 nT maximum. The total magnetic map reduced to equator (Figure 5b), when compared to the total magnetic intensity (TMI) (Figure 5a), the maps display similar anomaly in terms of anomalies trends, especially their symmetry, strike, extension, width, amplitude and gradients except for the magnetic low that occur within the north central portion of TMI map has now been reduced in size in the RTE map (Figure 5a and 5b). Also, the magnetic high that occurs just above this magnetic low within northern portion of TMI map has also been reduced in size in the RTE map (Figure 5a and 5b).

The Analytic Signal Map

The analytic signal map (Figure 6) accentuates the variation in the magnetization of the magnetic sources in the study area and highlights discontinuities and anomaly texture. These structures are observed around the North West and central portion of the area mostly trending NE-SW. The analytic signal amplitude maximizes over the edge of the magnetic structures as a result, the high magnetic anomalies zones are associated with

highly oxidized ferruginous chert nodules with some thin concretions (Gibson et al., 1999). Therefore, the MS zone (Figure 7b) has amplitude change from 0.02 to 0.15 m. The map could be the result of the combination of different magnetic zones with variable thickness and amplitude of the anomalies with the area of low intensity low magnetic zone (ML) with amplitude range of 0.02 to 0.15 m or more.

associated with highly oxidized rocks and areas with thick cover of sediment. The moderate magnetic zone (MM) with amplitude 0.04 to 0.47 m is associated with gneiss as these rocks contain high ferruginous with low amount of hematite. While the high magnetic zones with large amplitude (>0.47) could be attributed to highly magnetized rocks.



Figure 6: Magnetic Signal Map

Structural Complexity Analysis:
The algorithm of the FFT grid analysis was applied to the FFT map of the study area to produce the structural complexity maps which are standard deviation map. Vectorized structural map, contour correlation, density map and location history map.

intensity data of the study area. The pixel coloration within the north western portion of the map indicate high variation where areas with deep blue coloration indicate low variation in the magnetic intensity across the area (Figure 7a). Within the western half of the map, structures are signing predominantly in NE-SW direction while (Figure 7b) is a vectorized structural map gotten from standard deviation map.

The Standard Deviation Map:
The standard deviation map of the study area (Figure 7a) indicates variation in the magnetic

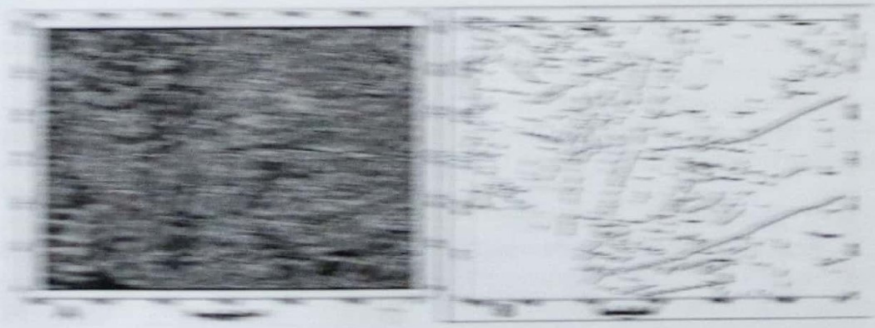


Figure 7: (a) Standard Deviation and (b) vectorized Structural Maps

From the vectorized structural map (Figure 7b), it can be observed that the area is highly fractured especially the north eastern portion of the map compare to the standard deviation where the portion is having high magnetic intensity variation attributed to freshly intruded rocks within the area. The central portion of the map is also highly faulted down to the southern portion of the map (Figure 7b). Predominant structural trend based on the vectorized structural map of the area is NE-SW and NW-SE.

The Contact Occurrence Density and Orientation Entropy Maps

The contact occurrence density map of the

study area (Figure 8a) was derived from the vectorized structural map of the area (Figure 7b) and it displays the number of fault/shear intersection and splays, that is where the linear structures intercept or changes direction and from (Figure 8a) it is evident that our contacts as displayed in the map showed where the structures either changes direction or intercepted by another structure and historically, those areas where the linear structures intercept or change directions are areas with high prospect for mineralization (Geosoft 2012; Holden *et al.* 2008).

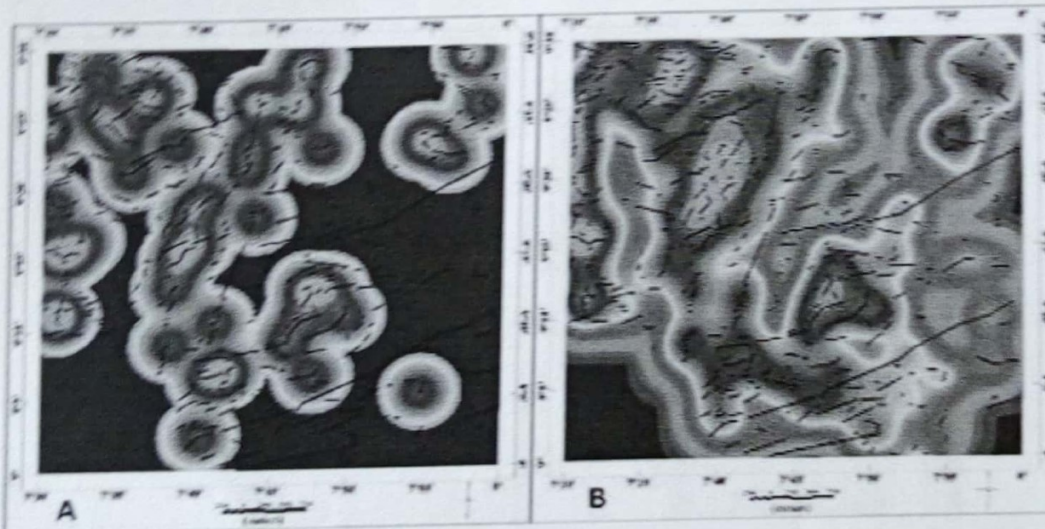


Fig. 8 (a) Contact Occurrence Density and (b) Orientation Entropy Maps

Also, the generated map of orientation entropy (Figure 8b) indicates high density zones of structural junctions or intersections. These are areas around the north eastern portion of the especially along the western edge and the central portion of the map (Figure 8b). These are areas presumed favorable for hosting deposits of interest which generally could be Gold, Pb-Zn mineralization, tin, iron ore, gemstone, Bismuth, Ilmenite and other minerals not discovered for now and could be further explored in more detail. It should be noted that this approach was originally designed to exploit a known deposits of

Archean Gold, but it may have some utility here since according to NGS (2006), there is occurrence of Gold in some part of FCT with Lead-Zinc mineralization. The extrapolation from an Archean case to the current situation in current study area could be useful since some part of the FCT falls in the study area (Figure 1 and Figure 3), it may host some of these minerals.

Percentage Potassium (%K), and Equivalent Thorium (eTh) Maps

The potassium (%K), map (Figure 9a) shows different degrees of potassium concentrations ranging from 0.219 to 5.088 (%) that reflects

different lithological units and alterations in the area. Potassium radiation fundamentally comes from potash feldspars, which are mainly common in felsic igneous rocks (e.g. granite) and are low in mafic rocks (e.g. basaltic and andesite) (Cunn *et al.* 1997b). Rock alterations can also result in high K concentrations (Wilford *et al.* 1997). A number of potassium anomalies are evident in the radiometric image (Figures 9a). The color blue corresponds with low K values whilst the pink corresponds with very high K values. The color red represents moderately high to high K values and the shades of orange to yellow color represent or are associated with moderately low K values. These pinkish colorations with very high K values within the eastern portion of the map are

attributed to the older granitoids (undifferentiated older granite and porphyritic granite). Also, figure 9b shows the eTh distribution map of the study area. The eTh distribution map has eTh concentration ranging from 6.389 to 36.159 ppm. For the purpose of this interpretation, the eTh concentration from the legend (figure 9b) in the study area will be relatively grouped as high (>22,304 ppm), corresponding mostly to the schist within north-eastern portion and Migmatite around the north with porphyritic granite around north-western portion of the map. While moderately high (13,925–22,304 ppm), moderately low (8,392–13,925 ppm), and low (<8,392 ppm) (figure 9b).

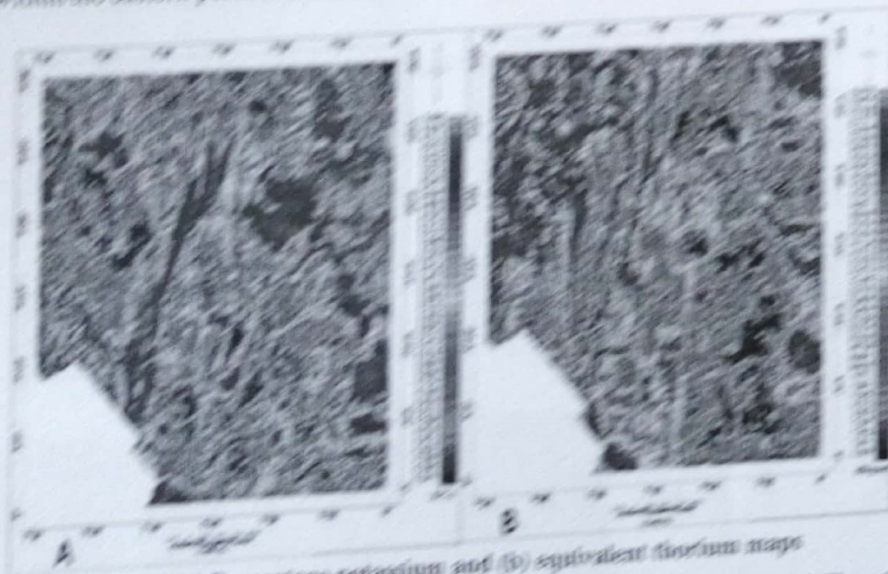


Fig. 9 (a) Percentage potassium and (b) equivalent thorium maps

Potassium/Thorium Ratio Map

Figure 10a displays K/eTh map and as potassium is more mobile than thorium, K/eTh ratio anomalies can be distinguished to areas of hydrothermal alteration which are characterized by K enrichment. However, depending on the fact that the ratio between potassium and thorium is rather constant in most rocks, typically varying from 0.17 to 0.2 K/Th in %ppm (Hoover *et al.* 1992). Rocks with K/eTh ratios remarkably outside of this range have been named potassium or thorium specialized (Portnoy 1987). So, the zones

characterized by the high K/eTh ratio values are the strong indicator of hydrothermal alteration. From the K/eTh ratio map (figure 10a) it is seen that the areas affected by the hydrothermal process is featured by pink color and have a high value about 0.385 of K/eTh ratio. These are areas associated with undifferentiated older Granite, Migmatite and gneiss with porphyritic granite in the east and some parts of Migmatite and pelitic schist/muscovite schist around southwestern portion of the map (figure 10b).

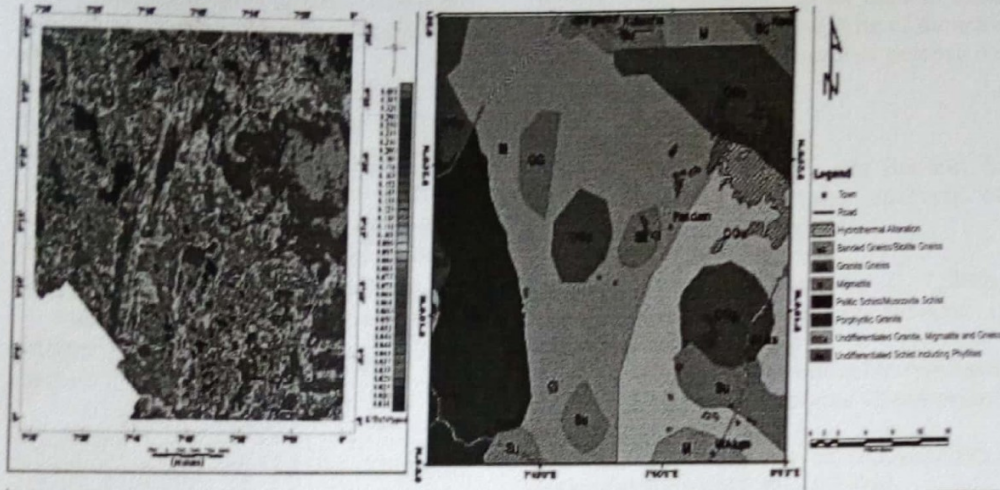


Fig. 10 (a) K/eTh and (b) hydrothermal Alteration Zones on Geologic map

Aeromagnetic and Aero Radiometric Data Integration

The results of aeromagnetic, aero radiometric data sets and geology were integrated to produce a composite map of the study area (figure 11). An inspection of this map showed some portions of the study that are highly faulted to be coincided with hydrothermal

alteration zone that is located within the area. Also, a number of hydrothermally altered zones are mapped from the K/eTh ratio map (figure 10b). Since these zones have one or more structures associations, they serve as channel pathways for migrating hydrothermal fluids that coincidentally reacted with rock formation which got altered subsequently.

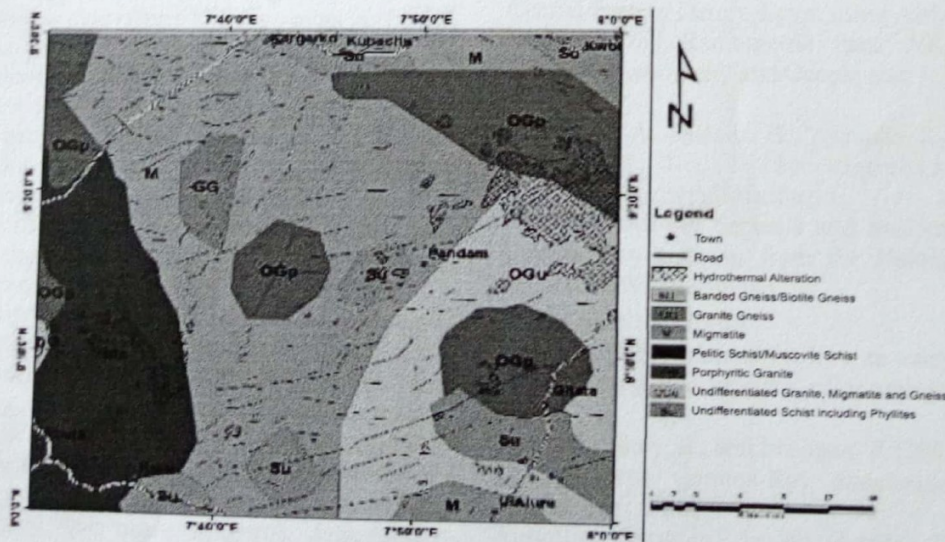


Fig. 11 Composite Proposed Geologic Map of the Area

- Decennial International Conference on Mineral Exploration, Australia*: 733-740.
- Holden, E. J., Dentith, M. and Kovesi, P. (2008). Towards the automatic analysis of regional aeromagnetic data to identify regions prospective for gold deposits. *Computers & Geosciences*, 34 (11): 1505-1513.
- Holden, E. J., Jason C. W., Kovesi, P., Daniel, W., Dentith, M., and Bagas, L. (2012). Identifying structural complexity in aeromagnetic data: An image analysis approach to greenfields gold exploration, *Ore Geol. Rev.* doi: 10.1016/j.oregeorev.2011.11.002
- Hoover, D. B., Heran, W. D., and Hill, P. L., 1992. The geophysical expression of selected mineral deposit models. U.S. Geological Survey Open-File report 92-557, 129p. Irvine, R.J., Smith, M.J., 1990. Geophysical exploration for epithermal gold deposits. *J. Geochem. Explor.* 36: 375-412.
- Irvine, R. J., and Smith, M. J., (1990). Geophysical exploration for epithermal gold deposits. *J. Geochem. Explor.* 36: 375-412.
- Kovesi, P. (1991). Image features from phase congruency", *Videre: Journal of Computer Vision Research, Summer*, 1(3), The MIT Press.
- Kovesi, P. (1997). Symmetry and asymmetry from local phase, AI'97, Tenth Australian. Joint Conference on Artificial Intelligence. 2 - 4.
- Morrell, A. E., Locke, C. A., Cassidy, J. and Mauk, J. L. (2011). Geophysical characteristics of adularia-sericite epithermal gold-silver deposits in the Waihi-Waitekauri region New Zealand. *Econ. Geol.*, 106: 1031-1041.
- NGSA. (2006). *Geology and Structural Lineament Map of Nigeria*
- Parker, J. R. (1997). *Algorithms for Image Processing and Computer Vision*. John Wiley & Sons Inc., USA: 417
- Portnov, A. M. (1987). Specialization of rocks toward potassium and thorium in relation to mineralization. *Int. Geol. Rev.* 29: 326-344.
- Roest, W., Verhoef, J. and Pilkington, M. (1992). Magnetic interpretation using 3-D analytic signal. *Geophysics*, 57: 116-125.
- Shives, R. B. K., Charbonneau, B. K. and Ford, K. L. (1997). The detection of potassic alteration by gamma ray recognition of alteration related to mineralization, in: *Exploration 97, Fourth Decennial International Conference*. Mineral Exploration (Toronto, Canada): 345-353.
- Telford, W. M., Geldart, L. P., Sherriff, R. E. and Keys, D. A. (1990). *Applied geophysics*. Cambridge: Cambridge University Press: 860.
- Wemegah, D. D., Preko, K., Noye, R. M., Boadi, B., Menyeh, A., Danuor, S. K., and Amenyoh, T. (2015). Geophysical interpretation of possible gold mineralization zones in Kyerano, South-Western Ghana using aeromagnetic and radiometric datasets. *J. Geoscience Environ. Prot.* 2015 (3): 67-82.
- Wilford, J. R., Bierwirth, P. N., and Craig, M. A. (1997). Application of Airborne Gamma ray Spectrometry in Soil/Regolith Mapping and Applied Geomorphology. *AGSO Journal of Australian Geology and Geophysics*, 17(2): 201-216.